NANO LETTERS

2007
Vol. 7, No. 7
2014−2019

Size-Dependent Angular Distributions of Low-Energy Photoelectrons Emitted from NaCl Nanoparticles

Kevin R. Wilson,[†] Shengli Zou,[‡] Jinian Shu,[§] Eckart Rühl,[||] Stephen. R. Leone,[†,⊥] George C. Schatz,[‡] and Musahid Ahmed*[,†]

Chemical Sciences Division, Lawrence Berkeley National Laboratory, Berkeley, California 94720, Department of Chemistry, Northwestern University, Evanston, Illinois 60208-3113, Research Center for Eco-Environmental Sciences, Chinese Academy of Sciences, Beijing, China, Institut für Chemie und Biochemie, Freie Universität Berlin, Takustr. 3, D-14195 Berlin, Germany, and Departments of Chemistry and Physics, University of California, Berkeley, California 94720

Received April 9, 2007; Revised Manuscript Received May 14, 2007

ABSTRACT

Angle-resolved threshold photoelectron spectra are recorded for size-selected beams of sodium chloride nanoparticles (radius = 25–250 nm). The photoelectron angular distributions exhibit a size-dependent asymmetry that is inversely proportional to particle radius. A model of the internal electric field amplitude and the photoelectron escape probability inside the particles reveals that the asymmetry in photoemission arises because the finite dimensions of the particle are comparable to both the photon penetration depth (14–22 nm) and electron escape length (10 nm).

Understanding the surface chemistry and photophysics of isolated nanoparticles is important for a variety of subjects that include solar cell engineering, atmospheric aerosols, and interstellar chemistry. Currently, there are only a few molecularly incisive methods for probing the surfaces of free nanoparticles. Mie, Raman,[1] and neutron[2] scattering methods probe the size, structure, and optical properties of microparticles and droplets; however extending some of these techniques to nanoparticles[1] remains challenging. Here we report a novel way to probe the surface electronic structure of isolated nanoparticles in a beam using vacuum ultraviolet (VUV) angle-resolved photoelectron spectroscopy.

Photoelectron spectroscopy (PES) is a surface-sensitive technique because of the shallow penetration depth of deep ultraviolet or X-ray radiation and the small escape lengths of the excited photoelectrons. In addition to solid and gas-phase samples, electron emission, produced by electrons or photons, is now used to probe complex samples such as soot in flames,[3] liquids,[4] aerosols,[5−7] and nanoparticles.[8,9] In a number of these studies, particle size is observed to play an important role in electron emission. For example, Ziemann et al.[10] found that for organic particles the secondary electron yield depends upon particle size. Schmidt-Ott and coworkers[11] found a 10−100 times enhancement of the bulk metal photoemission quantum yields in 4−10 nm diameter Ag and Au nanoparticles. In this Letter, we investigate nanoparticle photoemission and find that the photoelectron angular distributions of nanometer-sized NaCl aerosols depend on particle size and result primarily from the asymmetric electric field within the particle.

Velocity map imaging (VMI) is a sensitive method to obtain low kinetic energy angle-resolved photoelectron spectra. VMI allows the simultaneous measurement of the kinetic energy and angular distributions of ions or electrons originating from a photoionization event. It is commonly used to investigate the photoionization dynamics of atoms, molecules, and clusters.[12] Here we adapt a tunable wavelength VUV velocity map photoelectron imaging spectrometer to the study of nanoparticle photoemission. This approach is used to obtain the photoelectron spectra of sub-micrometer aerosol particles as well as to study the angular distribution of photoelectrons as a function of particle size. Recently, this technique was used by us to investigate electronic polarization effects in nanoparticles consisting of the amino acid glycine and the polypeptide phenylalanine−glycine−glycine.[13]

To determine how the angle-resolved photoemission spectrum depends upon particle size, photoelectron images

* To whom correspondence should be addressed. Phone: (510) 486-6355. Fax: (510) 486-5311. E-mail: mahmed@lbl.gov.
[†] Lawrence Berkeley National Laboratory.
[‡] Northwestern University.
[§] Chinese Academy of Sciences.
[||] Freie Universität Berlin.
[⊥] University of California.

10.1021/nl070834g CCC: $37.00
Published on Web 06/05/2007

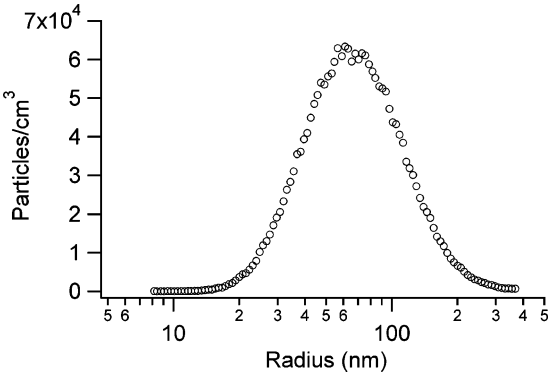

Figure 1. Particle size distribution produced by atomizing a 0.5 g/L aqueous solution of NaCl.

are recorded from monodisperse beams of NaCl nanoparticles. Nanoparticles are prepared by nebulizing or atomizing aqueous solutions of NaCl (0.5 g/L) in a carrier gas of nitrogen. Solid particles are formed as the droplets pass through a room-temperature diffusion dryer. Size selection and particle detection are performed using a commercial differential mobility analyzer (DMA, TSI 3081) and a condensation particle counter (TSI 3025A). The size distribution of NaCl aerosols obtained by these methods is shown in Figure 1. The broad distribution has a mean radius (R) of 78 nm and a total particle density of $\sim 1 \times 10^7$ particles/cm^3.

A focused nanoparticle beam is formed by passing the particles through a set of aerodynamic lenses (ADL),[14] yielding a beam diameter of $\sim$1.5 mm[15] in the interaction region of the spectrometer located 25 cm from the exit aperture of the ADL. The particle beam is skimmed twice after exiting the ADL to achieve a base pressure in the velocity map photoelectron spectrometer of 1×10^{-5} Pa. At the Advanced Light Source, tunable VUV radiation (7.5−30 eV) is generated by a 10 cm period undulator and dispersed by a 3 m normal incidence, off-plane Eagle monochromator located at the Chemical Dynamics Beamline. The particle beam is illuminated by an estimated flux of 10^{13} photons/s at 10 eV (15 meV bandwidth). Additional experimental details can be found in ref 13.

Synchrotron radiation intersects the nanoparticle beam at 90° forming a detection plane parallel to the velocity map imaging electron detector. The polarization of the undulator beam is horizontal and parallel to both the propagation direction of the particle beam and the plane of the electron detector, consisting of microchannel plates and a phosphor screen. The electron optics are biased to achieve "velocity map" conditions so that all electrons with the same momentum in the plane of the detector are imaged to the same position on the detector. The kinetic energy and angular distributions are extracted from the raw images using standard reconstruction methods. Here the photon beam propogation direction is the symmetry axis, since the photoelectron angular distributions are dominated by the vector normal to nanoparticle surface, rather than the polarization vector of the photon beam.

Shown in Figure 2 are the raw and reconstructed photoelectron images of a polydisperse NaCl beam, whose size

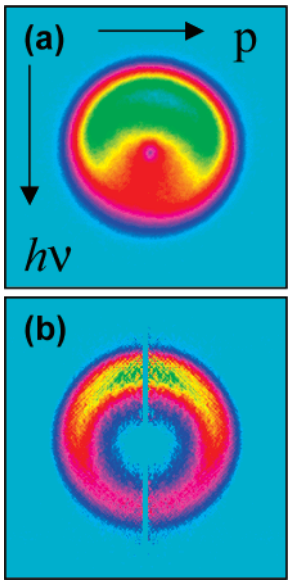

Figure 2. (a) Raw and (b) reconstructed velocity map photoelectron images of a polydisperse beam of NaCl particles recorded at a photon energy of 12 eV. Arrows indicate the propagation direction of the particle (p) and photon beams ($h\nu$).

distribution is shown in Figure 1. The images are recorded at a photon energy of 12 eV. Relative to both the propagation direction of the incoming photon ($h\nu$) and particle beams (p) there is a clear enhancement of photoelectron intensity emanating from the side of the particle beam directly illuminated by the incoming synchrotron radiation. A number of checks for possible artifacts such as detector inhomogeneity are performed. These tests indicate that the angular asymmetry does indeed originate from the asymmetric emission of electrons from the particle beam. It is important to emphasize that the asymmetric photoemission (denoted here as α) observed for nanoparticles is different from the anisotropy parameter (β) that normally describes photoionization events in gas-phase atoms, molecules, or clusters. A detailed analysis of the particle size dependence of this angular asymmetry (α) is considered below.

Shown in Figure 3a is the NaCl particle photoelectron spectrum obtained by radially integrating the reconstructed image shown in Figure 2. Kinetic energy calibrations of the electrons and the instrumental resolution are obtained using Xe gas. Despite the angular asymmetry, the photoelectron kinetic energy distributions in the forward and backward hemisphere are identical within the instrumental resolution. The photoelectron spectrum is similar to previous results reported for a NaCl thin film, which for comparison is also shown in Figure 3b.[16] There is a slight difference in the overall band profile obtained for particles compared to the thin film, with the latter (recorded at a photon energy of 75 eV) showing a distinct shoulder at $\sim$11.3 eV ionization energy. The valence band spectra of the alkali halides is interpreted as originating mainly from anion p levels (Cl 3p).[16] Currently, the reason for the lack of a clear shoulder toward higher energy in the particle phase photoelectron spectrum is unclear. This could result from morphological differences (e.g., density, crystalline vs amorphous) between

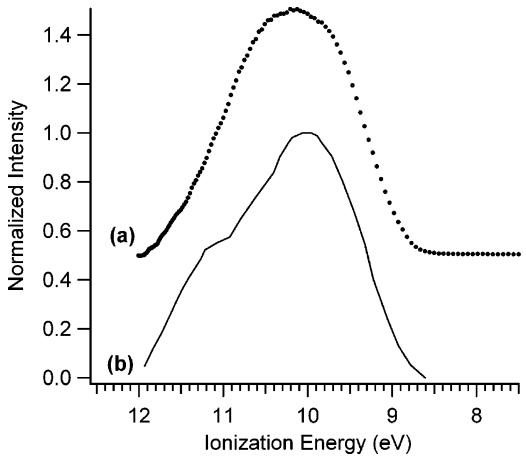

Figure 3. Photoelectron spectra of NaCl: (a) particles recorded at $h\nu = 12$ eV (y offset $= 0.5$) and (b) thin film[16] at $h\nu = 75$ eV.

thin films and particles or simply due to the instrumental resolution (0.25 eV) of the VMI spectrometer. Final state resonances in the conduction band accessed at 12 eV but not at 75 eV could also be responsible for differences in spectral intensity.

The center of the particle photoelectron band is located at an ionization energy of 10.2 eV and has a width of 1.8 eV, consistent with previous spectra recorded for NaCl surfaces.[16−18] A fit of the high kinetic energy side of the photoelectron band vs photon energy yields a straight line with an intercept of 8.2 ± 0.1 eV. This value corresponds to the valence band threshold for NaCl particles. This value is in good agreement with previous thin film studies[17] (8.1 eV) indicating that any electronic perturbation due to particle geometry is small. In addition, no size-dependent change in the particle phase photoelectron spectrum is observed, indicating that for the sizes investigated here no modification of the bulk-phase electronic structure occurs. More importantly, the close agreement of the photoelectron spectrum with previous thin film studies suggests that particle charging does not influence the absolute kinetic energy axis in these experiments. Clearly, using a continuously refreshed particle surface in this way eliminates sample charging and radiation damage that often complicate photoemission measurements of insulating samples at synchrotron light sources.

To examine how the asymmetry in angular photoemission depends upon the particle size, a DMA is used to produce a beam of monodisperse particles. The size selection is not perfectly monodisperse but has a full width at half-maximum of ~11 nm. Shown in Figure. 4 are raw velocity map images recorded as a function of both particle size and photon energy. In this figure the photon beam ($h\nu$) propagates from the top to the bottom of the image, while the particle beam (p) travels from left to the right in the plane of the image. The intense spot at the middle of the image corresponds to zero kinetic energy electrons, while the off-center bright spot in some of the images is an artifact that originates from background photoelectrons that are not well-focused under particle beam velocity mapping conditions. This aberration is also present in photoelectron images of pure Xe gas collected utilizing the same velocity map imaging system.

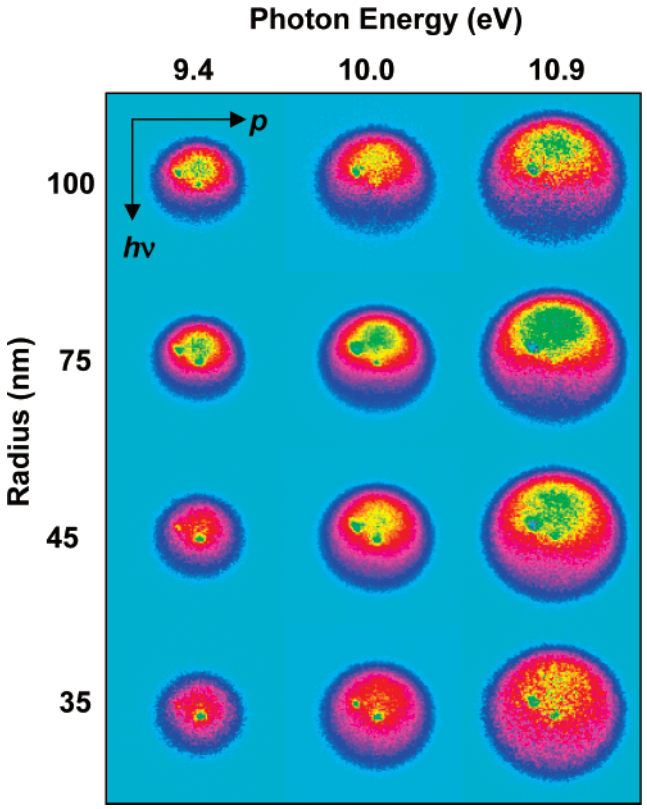

Figure 4. Raw photoelectron images of size-selected NaCl particles as a function of photon energy. Arrows indicate the propagation direction of the particle (p) and photon beams ($h\nu$).

There is a clear depletion of signal in the forward hemisphere with respect to the incoming photon beam. The magnitude of this asymmetry (α) can be quantified by taking the ratio of the integrated intensities in the forward and backward hemispheres. This is done by separately integrating the top and bottom halves of the reconstructed image. Equal intensity in the forward and backward hemispheres ($\alpha = 1$) corresponds to isotropic photoemission. An asymmetry ratio of 0.5 indicates that there is twice as much integrated intensity emanating from the top relative to the bottom of the image. In this case, more electrons are emitted in the backward direction along the axis of the incoming photon beam. In Figure 5, α ($h\nu = 10.9$ eV) is plotted vs R, the particle radius, revealing a clear particle-size dependence. The images become increasingly symmetric at small particle sizes. Images collected at other photon energies yield a similar dependence for α and are omitted for brevity. In general, similar angular patterns are observed, but not previously analyzed, for nanoparticle beams of insulators such as KI, SiO_2, oleic acid, glycine,[13] and phenylalanine−glycine−glycine[13] ionized at threshold. In contrast, metallic nanoparticles (Au and Ag) exhibit nearly symmetric photoemission that probably arises from the large differences in photoelectron dynamics in conductors, as will be considered in a forthcoming publication.

Plotting α vs R^{-1} yields a straight line also shown in Figure 5 (inset). A linear extrapolation of this plot predicts an asymmetry ratio of 1 (equal intensity in the forward and backward hemispheres) at $R = 24 \pm 4$ nm. From Lambert's

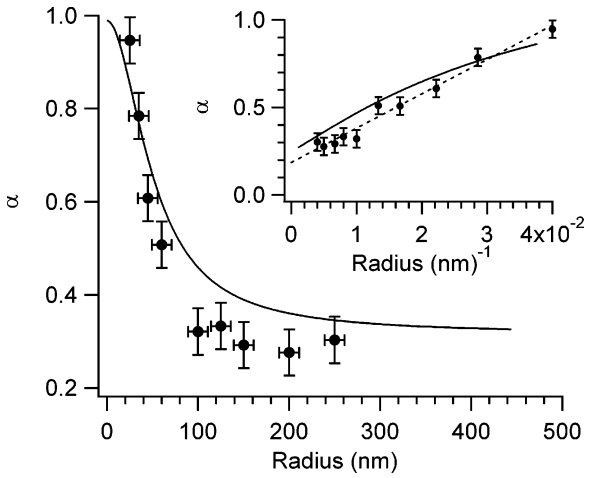

Figure 5. (●) Experimental asymmetry parameter, α, vs particle radius, *R*, at $h\nu = 10.9$ eV. (solid line) Model results using an index of refraction of $1.78 + 0.6i$ ($L_{abs} = 15$ nm) and an electron mean free path (r_{mfp}) of 10 nm. (Inset) Experimental values for α plotted vs inverse radius (R^{-1}) shown with a linear fit (dashed) and model results (solid).

law, the absorption length[19] (L_{abs}) for NaCl can be computed as

$$L_{abs} = \frac{\lambda}{4\pi\kappa} \quad (1)$$

where λ is the incident photon wavelength and κ is the imaginary component of the refractive index. For bulk NaCl at photon energies between 9 and 10 eV, κ increases from 0.5 to 0.7 yielding absorption lengths of 22 and 14 nm, respectively. These values are consistent with the experimentally derived photoabsorption lengths[19] of ~10−20 nm for evaporated films of CsI, KI, RbI, NaI, and CsBr at 8.8 eV.

Electron inelastic mean free paths depend upon kinetic energy and are well described by a "universal curve".[20] Electrons with kinetic energy between 30 and 1000 eV escape from depths between 2 and 50 nm. For low-energy electrons (<10 eV) the escape lengths are more uncertain due to electron−phonon interactions in the solid. Nevertheless, these escape lengths can range from a few to several hundred nanometers and are clearly expected to be on the order of the dimensions of the NaCl nanoparticles used in this study.

When the particle radius approaches the size of both the photoabsorption length and electron inelastic mean free path, isotropic ($\alpha = 1$) photoelectron emission is observed. Conversely, as the particle size exceeds both the photoabsorption and electron escape lengths, the images become more asymmetric, suggesting that only a fraction of the total particle volume (i.e., thin skin) is emitting photoelectrons. This interpretation is consistent with the linear relationship of α with R^{-1}, suggesting that the origin of the asymmetry reflects the increasing importance of surface layers with decreasing particle size.

To accurately describe photoemission from particles or small clusters, the effect of surface curvature is considered by numerous authors.[10,21−26] The confined geometry of nanometer-sized particles influences both the photoexcitation and the electron migration steps. The distance from the surface that electrons are produced by a photon is on average shorter for a curved surface than for a planar interface of a macroscopic sample. In a sphere, for example, this is simply due to the larger fraction of radiation striking the particle surface at oblique or grazing angles. Similarly, at a given creation depth, photoelectrons migrate over shorter distances to reach the curved particle surface compared with a bulk sample and a planar boundary. These geometric effects depend upon particle size and at least in part have led to enhanced secondary electron yields of organic aerosols[10] as well as photoelectron quantum yields in metallic nanoparticles.[11]

To further examine how geometry influences the photoabsorption and electron migration steps and to understand in more detail the relationship between α and *R*, a model for particle photoemission is developed. Our approach is similar to the one first developed by Watson.[21] For the model, the NaCl nanoparticles are approximated as spheres so that Mie theory can be used to calculate the electromagnetic field, *E*, inside a spherical nanoparticle that gives rise to photoemission. A cubic grid of 100 × 100 × 100 points is defined so that the particle exactly fits inside a box of 100 on a side. For each point (*x*, *y*, *z*) on the grid and inside the particle, the intensity factor $|E(x,y,z)|^2$, computed via Mie theory, is used to estimate the photoexcitation probability. Shown in Figure 6 are contour plots that indicate the electric field amplitude ($|E|^2$) as a function of particle radius (r_{max}). For particle radii of 100 nm and larger, $|E|^2$ is strongly peaked on the side of the particle directly illuminated by the incoming photon beam. In this case, there is a strong preference for photoelectrons to be emitted in the backward direction, simply reflecting the strong asymmetry in the electric field. As the particle size decreases, the photon beam penetrates more deeply into the material providing a more uniform photoexcitation probability. For example in a 5 nm radius particle, $|E|^2$ is uniformly distributed throughout the entire particle indicating that photoemission would be nearly isotropic.

To compute α as a function of particle size using the field contours shown in Figure 6, the photoelectron originating from a position whose coordinates are *x*, *y*, *z* is assumed to be emitted at random polar and azimuthal angles θ and ϕ (sampled from a uniform 20 × 20 grid) relative to the polarization direction. The polarization direction is averaged over the three Cartesian directions (taken to be *x*, *y*, and *z*) in determining the overall emitted photoelectron intensity. For a given θ and ϕ, the photoelectron intensity is assumed to be weighted by $\sin^2\delta\, e^{-d/r_{mfp}}$, where the $\sin^2\delta$ factor is the intensity expected for dipole excitation. δ is the angle between the polarization direction and the outgoing electron. The factor $e^{-d/r_{mfp}}$ is the attenuation function for a photoelectron traveling along a length *d* between the coordinate *x*, *y*, *z* and the sphere surface. r_{mfp} is the electron mean free path. Thus the overall expression for the averaged photoemission intensity in the forward direction is given by

$$f_{forward} = \sum_{pol=x,y,z} \sum_{x,y,z} \sum_{\theta=0}^{90^\circ} \sum_{\phi=0}^{360^\circ} |E(x,y,z)|^2 e^{-d/r_{mfp}} \sin^2\delta \sin\theta \quad (2)$$

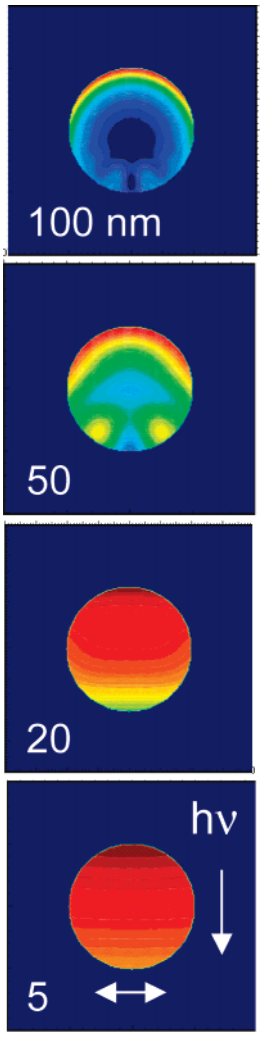

Figure 6. Contour plots, obtained via Mie theory, show the electric field amplitudes, $|E|^2$, inside 100, 50, 20, and 5 nm radius particles. Red corresponds to regions of high $|E|^2$ inside the particle. Arrows indicate both the polarization vector and the propagation direction of the photon beam ($h\nu$).

where sin θ is the weight associated with integration over the polar angle. The corresponding backward intensity f_{backward} is an average over θ from 90° to 180°, which is used to compute $\alpha = f_{\text{forward}}/f_{\text{backward}}$. To obtain α as a function of particle radius, r_{max}, it is straightforward to show that the distance the photoelectron travels (d) is related to the variables x, y, z, θ, ϕ, and r_{max} via

$$d = -G + \sqrt{G^2 + {r_{\text{max}}}^2 - x^2 - y^2 - z^2} \qquad (3)$$

where

$$G = x \sin\theta \cos\phi + y \sin\theta \sin\phi + z \cos\theta \qquad (4)$$

In reality, the experimental NaCl particles are nonspherical. The experimental radius (R) in Figures 1 and 5 is assumed to correspond to half the edge length of a perfect cubic crystal of NaCl. Since spherical particles are used in the Mie theory calculations, r_{max} is transformed to the experimental R by simply equating the projected areas of a sphere, $\pi {r_{\text{max}}}^2$, with that of a cube $(2R)$.[2] This yields $r_{\text{max}} = (4/\pi)^{1/2}R$. While there may be some error in assuming that the orientational average of cubes may be related to spheres, this transformation provides a somewhat more realistic comparison of theory with experiment than taking $r_{\text{max}} = R$. In the past, some deviations from cubic structure have been observed in micrometer-sized NaCl particles.[27] For the results presented here, this is not expected to change the main conclusions drawn from the model.

Figure 5 shows α versus R computed using eq 2 and Mie theory calculations using an index of refraction of $1.78 + 0.6i$ taken from Miyata and Tomiki.[28] At 10.9 eV this corresponds to an absorption length of 15 nm. In general, Figure 5 shows that the model results are in reasonable agreement with the measurements, with the transition from $\alpha = 1$ to $\alpha < 0.5$ occurring between radii of 40 and 100 nm. Electron attenuation plays a critical role in determining the model results in Figure 5, with the 10 nm electron migration length yielding the best agreement with experiment on average. A mean free path of 10 nm is consistent with the range of values previously computed by Akkermann.[29] Smaller values of r_{mfp} tend to underestimate the experimental α for $R < 40$ nm, while larger r_{mfp} overestimate α for $R >$ 100 nm. Given the uncertainties in the model, such as the assumption of a unit transmission coefficient when the electron strikes the particle surface and spherical particles, the quality of the agreement between theory and experiment is quite reasonable.

VMI of nanoparticle beams reveal that although 25−250 nm NaCl particles exhibit bulklike electronic properties, there is a strong angular asymmetry in the photoemission that depends upon particle size. For insulating particles, α is observed to be linear with inverse radius, which reflects the increasing importance of particle size relative to the photoabsorption and electron migration lengths. Metallic nanoparticles, such as gold, have similar refractive indices as NaCl in the VUV, yet the electron dynamics in conductors may produce very different photoelectron angular distributions than insulators. Preliminary results indicate that this is indeed the case.

Additional experimental studies are underway to examine how an organic film on a NaCl particle influences the photoelectron angular distribution and the photon penetration depth. These experiments are designed to utilize the surface sensitivity of PES to address more challenging aspects of particle-phase heterogeneous tropospheric chemistry such as the oxidative aging of organic aerosol surfaces. Furthermore, measuring angle-resolved photoemission spectra of silicate or graphite aerosols coated with ice or aromatic hydrocarbons could provide a more realistic proxy for understanding the complex role of dust grains in the photoelectron heating of interstellar clouds.[30]

For a cube there are no known analytic solutions for Maxwell's equations. As a result, a simpler model of photoemission was used here instead. This approach, based upon the Mie theory of spherical particles, captures the overall functional form of α versus particle radius and reveals

that the internal electric field distribution inside the particle plays a large role in producing the photoelectron angular patterns observed in the experiment. The model provides confirmation of the underlying physics of asymmetric particle photoemission and its dependence upon particle size. Not surprisingly, however, there remain some discrepancies between the model and experiment as illustrated in Figure 5. To resolve these differences, more sophisticated numerical approaches,[31] such as the discrete dipole approximation, could be used to investigate more subtle features of photoemission in nonspherical nanometer-sized objects. For example, cube corners or edges can produce enhanced photoemission due to higher $|E|^2$ in these geometric regions. As such, spherical particles may not accurately account for the magnitude of these enhancements even when a random ensemble of cubes is probed in a nanoparticle beam.

When combined with nanoparticle beams, VMI provides a new way to probe the surfaces of condensed matter using techniques originally designed for gas-phase atoms, molecules, and clusters. Furthermore, particle beams are a source of continuously replenished surfaces that eliminate sample charging and radiation damage that often complicate traditional photoelectron-based surface science methods. All of this is particularly important for probing the electronic structure of nanoparticles in the absence of substrates, with potential new applications in characterizing nanomaterials, environmental and aerosol surfaces, as well as the photophysics of interstellar grains.

Acknowledgment. This work was supported by the Director, Office of Science, Office of Basic Energy Sciences, Chemical Sciences Division of the U.S. Department of Energy under Contract No. DE-AC02-05CH11231. G.C.S. and S.Z. acknowledge DOE Grant DEFG02-02-ER15487. E.R. acknowledges financial support by the BMBF (Contract No. 05 KS4WW1/7) and the Fonds der Chemischen Industrie.

References

(1) Reid, J. P.; Mitchem, L. *Ann. Rev. Phys. Chem.* **2006**, *57*, 245.
(2) Wyslouzil, B. E.; Wilemski, G.; Strey, R.; Heath, C. H.; Dieregsweiler, U. *Phys. Chem. Chem. Phys.* **2006**, *8*, 54.
(3) Mitchell, J. B. A.; Rebrion-Rowe, C.; Legarrec, J. L.; Taupier, G.; Huby, N. *Combust. Flame* **2002**, *131*, 308.
(4) Bluhm, H.; Ogletree, D. F.; Fadley, C. S.; Hussain, Z.; Salmeron, M. *J. Phys.: Condens. Matter* **2002**, *14*, L227.
(5) Janssen, E.; Goldmann, A. *J. Electron Spectrosc. Relat. Phenom.* **1993**, *63*, 327.
(6) Burtscher, H.; Scherrer, L.; Siegmann, H. C.; Schmidt-Ott, A.; Federer, B. *J. Appl. Phys.* **1982**, *53*, 3787.
(7) Ziemann, P. J.; McMurry, P. H. *Aerosol Sci. Technol.* **1998**, *28*, 77.
(8) Grimm, M.; Langer, B.; Schlemmer, S.; Lischke, T.; Becker, U.; Widdra, W.; Gerlich, D.; Flesch, R.; Rühl, E. *Phys. Rev. Lett.* **2006**, *96*, 066801.
(9) Fierz, M.; Siegmann, K.; Scharte, M.; Aeschlimann, M. *Appl. Phys. B* **1999**, *68*, 415.
(10) Ziemann, P. J.; Liu, P.; Kittelson, D. B.; McMurry, P. H. *J. Phys. Chem.* **1995**, *99*, 5126.
(11) Schmidt-Ott, A.; Schurtenberger, P.; Siegmann, H. C. *Phys. Rev. Lett.* **1980**, *45*, 1284.
(12) Eppink, A. T. J. B.; Parker, D. H. *Rev. Sci. Instrum.* **1997**, *68*, 3477.
(13) Wilson, K. R.; Peterka, D. S.; Jimenez-Cruz, M.; Leone, S. R.; Ahmed, M. *Phys. Chem. Chem. Phys.* **2006**, *8*, 1884.
(14) Liu, P.; Ziemann, P. J.; Kittelson, D. B.; McMurry, P. H. *Aerosol Sci. Technol.* **1995**, *22*, 314.
(15) Wilson, K. R.; Jimenez-Cruz, M.; Nicolas, C.; Belau, L.; Leone, S. R.; Ahmed, M. *J. Phys. Chem. A* **2006**, *110*, 2106.
(16) Wertheim, G. K.; Rowe, J. E.; Buchanan, D. N. E.; Citrin, P. H. *Phys. Rev. B* **1995**, *51*, 13675.
(17) Taylor, J. W.; Hartman, P. L. *Phys. Rev.* **1959**, *113*, 1421.
(18) Poole, R. T.; Jenkin, J. G.; Liesegang, J.; Leckey, R. C. G. *Phys. Rev. B* **1975**, *11*, 5179.
(19) Boutboul, T.; Breskin, A.; Chechik, R.; Braem, A.; Lion, G. *J. Appl. Phys.* **1998**, *83*, 7896.
(20) Seah, M. P.; Dench, W. A. *Surf. Interface Anal.* **1979**, *1*, 2.
(21) Watson, W. D. *J. Opt. Soc. Am.* **1973**, *63*, 164.
(22) Dionne, G. F. *J. Appl. Phys.* **1973**, *44*, 5361.
(23) Chen, Q. Y.; Bates, C. W. *Phys. Rev. Lett.* **1986**, *57*, 2737.
(24) Bottigli, F.; Coutant, J.; Fois, M. *Phys. Rev. A* **1972**, *6*, 1830.
(25) Ballester, J. L.; Shi, Y.; Dwek, E. *J. Opt. Soc. Am. B* **1995**, *12*, 1211.
(26) Müller, U.; Burtscher, H.; Schmidt-Ott, A. *Phys. Rev. B* **1988**, *38*, 7814.
(27) Berge, B.; Sudholz, K.; Steiner, B.; Rohmann, J.; Rühl, E. *Phys. Chem. Chem. Phys.* **1999**, *1*, 5485.
(28) Miyata, T.; Tomiki, T. *J. Phys. Soc. Jpn.* **1968**, *24*, 1286.
(29) Akkerman, A.; Boutboul, T.; Breskin, A.; Chechik, R.; Gibrekhterman, A. *J. Appl. Phys.* **1994**, *76*, 4656.
(30) Draine, B. T. *Ann. Rev. Astron. Astrophys.* **2003**, *41*, 241.
(31) Mishchenko, M. I.; Hovenier, J. W.; Travis, L. D. *Light Scattering by Nonspherical Particles*; Academic Press: San Diego, 2000.

NL070834G